Next Materials 7 (2025) 100363

Contents lists available at ScienceDirect

Next Materials

journal homepage: www.sciencedirect.com/journal/next-materials

Research article

CALPHAD approach for prediction of local phase transformation at superlattice stacking fault in gamma prime precipitates in superalloys with multi-component system

Takuma Saito [a,b,*,1], Hiroshi Harada [a,2], Taichi Abe [a], Hideyuki Murakami [a,b]

[a] National Institute for Materials Science, 1-2-1 Sengen, Tsukuba 305-0047, Japan
[b] Department of Nanoscience and Nanoengineering, Waseda University, 3-4-1 Okubo, Shinjuku, Tokyo 169-8555, Japan

ARTICLE INFO

Keywords:
Superalloys
Stacking fault
Solute partition
Local phase transformation
Suzuki effect

ABSTRACT

This manuscript investigated the possibility of CALPHAD (calculation of phase diagram) approach to predict the local phase transformation (LPT) accompanied by compositional transition on the superlattice stacking fault in the γ' precipitates in multi-component superalloys. The method is basically parallel tangent construction using the concept of the LPT phase in the system of γ and γ' phases to approximate the atomic structure of the stacking fault. Because the important issue for the strengthening by the LPT is whether the LPT phase is ordered or disordered, the ordering was judged by the size of the stacking fault energy to form the LPT phase from γ' precipitates. In addition, since the solute partitioning ratio between LPT phase and γ' precipitates is also significant to consider the LPT, the predicted ratio was verified using the experimental results in the previous reports. In the case of SISF (superlattice intrinsic stacking fault), Co-base superalloys tend to form ordered χ LPT phase, but formability of ordered χ and disordered ε LPT phases in Ni-base superalloys is calculated to be competitive. The predicted solute partitioning rate almost agrees with the experimental one except for Nb in multi-component superalloys. This discrepancy could originate from the accuracy of the physical properties of Ti and Nb in the database of χ LPT phase. In the case of SESF (superlattice extrinsic stacking fault), all considered alloys of Ni-base superalloys were predicted to have ordered η LPT phase, judged by stacking fault energy, however, the predicted solute partitioning ratio was different from the experimental ones. This issue could originate from inaccurate physical properties between Ti and Ta in the database of η LPT phase with the multi-component system.

1. Introduction

Ni-base superalloys have been required to have superior creep properties at higher temperatures to enhance the thermal efficiency of land-based gas turbine and jet engines. The origin of creep properties of Ni-base superalloys is an activity of dislocations in the microstructure consisting of γ (disordered solid solution face-centered cubic structure) and γ' (ordered $L1_2$ structure) two phases. Especially during creep at an intermediate temperature and high applied stress in single-crystal alloys, the formation and propagation of dislocations with a stacking fault such as dislocation ribbon [1] and microtwin [2] which can shear γ' precipitates dramatically degrade the creep properties. Therefore, a new alloy design approach to impede the formation and propagation of such dislocations has been sought for a long time. A key to solving this problem is control of atomic arrangement at the stacking fault of γ' precipitates. Especially in turbine disk superalloys, a guideline of alloy design to form an ideal atomic arrangement at the stacking fault has been established [2,3].

In the case of disordered solid solution alloys with FCC structure, Hideji Suzuki proposed the strengthening mechanism of a solid solution called “Suzuki effect” later [4]. Suzuki effect assumes that almost all the dislocations in solid solution FCC alloys should have partial dislocations separated by a small width of an intrinsic stacking fault [5,6] whose atomic stacking is equivalent to that of a hexagonal close-packed (HCP)

* Corresponding author at: National Institute for Materials Science, 1-2-1 Sengen, Tsukuba 305-0047, Japan.
E-mail address: Takuma.Saito@ruhr-uni-bochum.de (T. Saito).
[1] Present address: Ruhr-University Bochum, Universitatstrsse 150, Bochum, 44780, Germany
[2] Present address: Superalloys Design Laboratory, 3–18-33 Azuma, Tsukuba, 305–0031, Japan

https://doi.org/10.1016/j.nxmate.2024.100363
Received 19 June 2024; Received in revised form 26 August 2024; Accepted 27 August 2024
Available online 5 September 2024

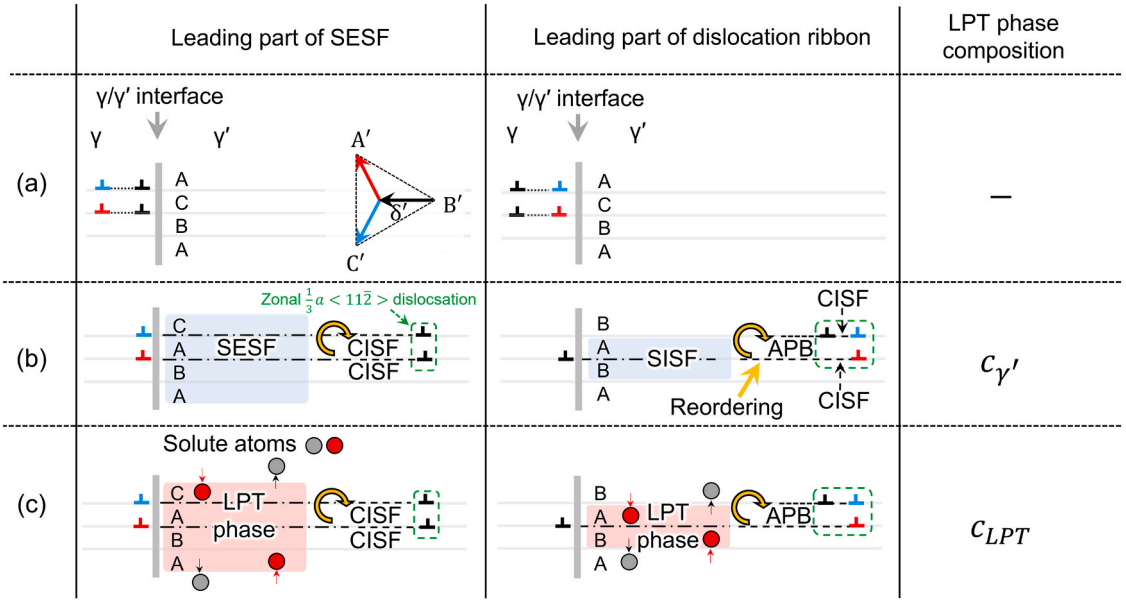

Fig. 1. Schematic summary for simple understanding of the process to form the LPT phase in SESF and SISF belonging to the leading part of dislocations. Number of atomic layers of LPT phase is described as number of atomic layer necessary for LPT embryo at stacking fault [36]. (a) before shearing γ' precipitates by dislocations, (b) shearing γ' precipitates with stacking fault by dislocations via reordering atoms, (c) LPT formation at the stacking fault.

structure [4]. Immediately after the formation of the stacking fault with the same composition as that of the FCC matrix, solute elements in FCC matrix and the stacking fault with HCP structures have different chemical potential since each region has the same composition [4]. In the thermal equilibrium condition, the solute elements are re-partitioned to reach the same chemical potential in each region [4]. Recently, the local change of composition at the stacking fault by Suzuki effect has been referred to local phase transformation (LPT) [7].

In the case of ordered $L1_2$ structure which is equivalent to γ' phase, atomic arrangement at the stacking fault by LPT has been reported to be either ordered or disordered phases [2,3,8], which is different from the case for the alloys which Suzuki effect originally assumes. Based on knowledge proofed by recent research using energy-dispersive X-ray spectroscopy (EDS) in scanning transmission electron microscope (STEM) [2,3,7–25] and atom probe tomography (APT) [8,19,24,26–28], the new alloy design approach for Ni-base superalloys has been developed by forming ordered LPT phase such as χ phase at superlattice intrinsic stacking fault (SISF) [3] and η phase at superlattice extrinsic stacking fault (SESF) [2] rather than disordered LPT phase by modifying nominal composition. Therefore, prediction of LPT phase by modifying nominal composition should be important for development of superalloys with superior mechanical strength.

For the prediction of LPT phase, the density function theory (DFT) calculation has been generally conducted for simple compositional models such as binary and ternary systems [29–31]. However, the DFT calculation is difficult to predict the LPT phase in a multi-component system to which almost all the Ni-base superalloys belong. To resolve this difficulty, calculation of phase diagram (CALPHAD) approach is used to predict LPT phase based on Suzuki effect. This approach has been proposed in Mg-Zn-Y system [32] and Ni-base superalloys [33,34]. However, the accuracy and prediction results by this framework have not been investigated, especially for superalloys. Therefore, this

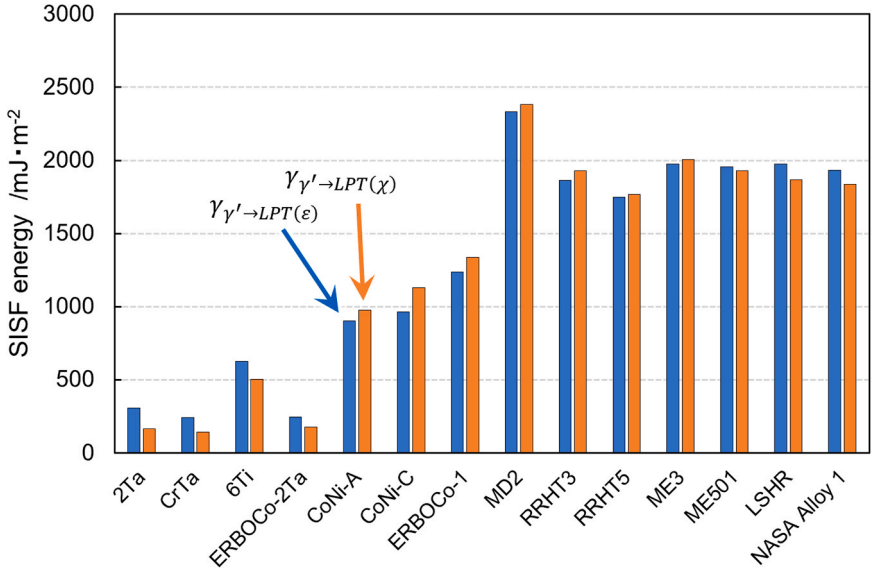

Fig. 2. SISF energy to form LPT phase in γ' precipitates after the event of Suzuki effect.

research aimed to confirm the accuracy and prediction results by CALPHAD approach for LPT phase with solute partition in more vast superalloy range such among Ni-base superalloys, Co-base superalloy, and CoNi-base superalloys in comparison with previous experimental works, with our own ideas.

2. Theory/calculation

Fig. 1 summarizes the assumed steps until the LPT phase is formed in the early stage of nucleation and propagation of the dislocation ribbon and the microtwin. We assume that super-partial dislocation with superlattice stacking fault is formed at γ/γ' interface from two perfect dislocations in the γ matrix belonging to neighboring slip planes, and the super-partial dislocation with the stacking fault is propagated into γ' precipitates, as schematically shown in Fig. 1. In the region of γ' precipitates where leading $\frac{1}{3}a < 11\overline{2} >$ super partial, called zonal $\frac{1}{3}a < 11\overline{2} >$ dislocation in this manuscript, belonging to the dislocation ribbon or the microtwin has sheared as shown in Fig. 1(b), reordering atoms via vacancy motion has to occur to create superlattice intrinsic stacking fault (SISF) or superlattice extrinsic stacking fault (SESF), to remove Al-Al nearest neighbor bonding from two layered planar defects such as APB/CISF or CISF/CISF parts [35], where CISF is short for complex intrinsic stacking fault and APB is short for anti-phase boundary, and CISF/CISF part is called complex extrinsic stacking fault (CESF). Then, solute atoms at SISF or SESF are arranged by Suzuki effect to meet the equilibrium condition with the diffusion of atoms around the planar defects. The formation of LPT phase could change the kinetics of further motion of dislocations to which the stacking fault belongs [2,3]. The kinetics of dislocations with LPT phase is reported to be rate-controlled by kinetic of Cottrell atmosphere formation around a core of the leading dislocation [14] or diffusion of heavy elements such as W from surrounded γ' precipitates [16] because the formation of LPT phase requires solute elements from such sources. Notably, this manuscript focuses only on the first and final steps to form LPT phase described in Fig. 2, (a) and (c) under the assumption that the solute partition is formed immediately after the formation of stacking faults [31]. This manuscript only refers to the formed LPT phase and its composition rather than kinetics of the formation.

In this manuscript, a possible formed LPT phase was predicted in CALPHAD approach using a database for Ni-base alloys by comparing stacking fault energy. Since stacking fault exists in γ' precipitates which is nucleated at γ/γ' interface from two perfect dislocations in γ matrix, stacking fault energy in this manuscript is equivalent to formation energy of stacking fault in γ' precipitates via activity of dislocations. In this point of view, LPT phase with a lower stacking fault energy is preferred to form because its formation energy is lower than the other. Notably, stacking fault energy does not directly refer to mechanical strength in this manuscript since the mechanical strength such as creep strength can be also determined by the kinetics of LPT phase formation by diffusion of atoms. Furthermore, the framework of this idea to predict preferred LPT phase by the stacking fault energy is based on thermal equilibrium condition rather than kinetic, which can be estimated by activation energy. To calculate stacking fault energy, Eq. (1) was used [36], where ρ_A^{LPT} and $\rho_A^{\gamma'}$ are the atomic density per area in LPT phase and the γ' phase, G_{LPT} is Gibbs free energy of the LPT phase whose composition is after the Suzuki effect, and $G_{\gamma'}$ is Gibbs free energy of original γ' phase, and n is a number of atomic layer thick plates with embryo of LPT phase beneath staking fault [36] sandwiched by $L1_2$ phase. n is calculated by $n = x \bullet m$, where dislocation per x atomic layer reproduces the bulk LPT phase and such m dislocations reproduces the embryo of the LPT phase, in the original definition [36]. Assuming the situation shown in Fig. 1, The motion of one zonal $\frac{1}{3}a < 11\overline{2} >$ dislocation in every two atomic layers reproduces the bulk LPT phase (n=2, x=2, m=1 in the case of SISF), and the motion of one zonal $\frac{1}{3}a < 11\overline{2} >$ dislocation in every four atomic planes reproduces the bulk LPT phase (n=4, x=4, m=1 in the case of SESF). Therefore, this manuscript treats that n of LPT phases at SISF is 2, and that of LPT phases at SESF is 4, respectively, as depicted in Fig. 1. The detailed procedure how to estimate n value is described in Appendix part.

Table 1
Relationship between a lattice constant and a closed-pack distance in the phases.

Physical parameters	γ	γ'	ε	χ	ε'	η
Number of atoms in the unit cell c	4		6		12	
Lattice constant a	$v^{\frac{1}{3}}$		$\left(\frac{2^{\frac{1}{2}}\cdot v}{6}\right)^{\frac{1}{3}}$		$\left(\frac{2^{\frac{1}{2}}\cdot v}{12}\right)^{\frac{1}{3}}$	
Distance between the closed-pack plane d_{CPP}	$\frac{3^{\frac{1}{2}}}{3}\cdot a$		$\frac{6^{\frac{1}{2}}}{3}\cdot a$		$\frac{6^{\frac{1}{2}}}{3}\cdot a$	

$$\gamma_{SFE(\gamma'\rightarrow LPT)} = n\cdot\left(\rho_A^{LPT}\cdot G_{LPT} - \rho_A^{\gamma'}\cdot G_{\gamma'}\right) \quad (1)$$

Notably, for simple discussion, Eq. (1) ignores the effect of elastic energy and surface energy on stacking fault energy. This treatment is reasonable because the previous work reported that a difference in Gibbs free energy between the phases is significantly more dominant in the stacking fault energy than any other terms [37]. For calculating ρ_A^{LPT} and $\rho_A^{\gamma'}$, Eq. (2) was used, where ρ_v is molar volume and d_{CPP} is a distance between closed packed planes in the phase.

$$\rho_A = \rho_v\cdot d_{CPP} \quad (2)$$

To estimate d_{CPP}, the relationship between volume in a unit cell of a phase and lattice constant was used. Eq. (3) can calculate a volume in the unit cell v, where V is a molar volume that can be estimated using CALPHAD calculation in a relation $V = \frac{1}{\rho_v}$, c is the number of atoms in the unit cell, and N is the atomic number in 1 mol. For each phase in this manuscript, physical parameters in Table 1 were used.

$$v = V\cdot\frac{c}{N} \quad (3)$$

The predicted LPT phase and its composition were compared with previously reported experimental results using STEM-EDS and APT analysis about a series of Co-base, CoNi-base, and Ni-base superalloys. Table 2 shows the nominal composition of each alloy used in CALPHAD calculation in this manuscript. Notably, minor elements such as Zr, B, and C were not considered in this research.

For CALPHAD calculation, ThermoCalc 2023a with a database of TCNI11: Ni-Alloys v11.0 was used. To approximate a crystal structure and ordering of solute atoms in the stacking fault using phase data, LPT phases were assumed. A relationship between detailed information on LPT phases and phase data in TCNI11 is listed in Table 3. This research assumed ε and χ phases to approximate the LPT phase formed at SISF, furthermore, ε' and η phases to approximate the LPT phase formed at SESF. It should be noted that HCP_A3 was also used to approximate ε' phase under an assumption that there is little difference in thermodynamic properties between ε and ε' phases. Among the LPT phases in the calculation, sublattice was taken into consideration only in $D0_{19}$ adapting to χ phase, $D0_{24}$ adapting to η phase to reproduce the ordering of solute atoms.

To estimate the physical parameters of the LPT phases and solute partition both before and after the event of Suzuki effect, calculation using the system of γ, γ', and LPT phases was conducted. The nominal composition shown in Table 2 was used in the calculation. Before the calculation, phase data of γ and γ' phases were set in "enter", while that of the LPT phases were set in "dormant". This means that equilibrium compositions of the phases with "enter" are calculated so as to minimize total Gibbs free energy of the system using phase date with the state of "enter". Notably, the composition of a phase with a state of "dormant" was calculated so as to minimize Gibbs free energy of the phase keeping the same chemical potential and total Gibbs free energy obtained in the

Table 2
Composition and conditions of alloys used in CALPHAD calculation except for minor elements (at%).

Alloys	Ni	Co	Cr	Mo	W	Al	Ti	Ta	Nb	Temperature /°C	Class	Reference
2Ta	-	79.40	-	-	9.80	8.80	-	2.00	-	900	Co-base	[9]
CrTa	-	78.40	4.50	-	7.80	7.80	-	1.50	-	900	Co-base	[9]
6Ti	-	79.00	-	-	8.10	6.70	6.20	-	-	900	Co-base	[9]
ERBOCo−2Ta	-	81.50	-	-	7.50	9.00	-	2.00	-	975	Co-base	[28]
CoNi-A	29.20	45.90	6.40	-	6.30	9.80	-	2.40	-	900	CoNi-base	[12]
CoNi-C	38.00	38.00	6.40	-	6.90	9.30	-	1.40	-	900	CoNi-base	[9]
ERBOCo−1	32.00	45.00	6.00	-	5.00	8.00	2.50	1.50	-	850	CoNi-base	[26]
MD2	66.60	9.30	5.30	1.30	2.60	11.20	1.70	2.00	-	800	Ni-base	[15]
RRHT3	51.10	18.10	14.00	1.50	0.80	8.00	-	1.00	5.50	750	Ni-base	[24,38]
RRHT5	50.00	18.30	14.00	1.50	0.80	9.80	-	1.00	4.60	750	Ni-base	[38]
ME3	49.66	20.13	14.39	2.28	0.66	7.47	4.09	0.76	0.56	760	Ni-base	[2,3]
ME501	52.50	18.15	13.71	1.80	0.97	6.61	3.72	1.58	0.96	760	Ni-base	[2,16]
LSHR	49.81	20.08	13.94	1.63	1.36	7.52	4.24	0.48	0.94	760	Ni-base	[3]
TSNA−1	52.06	19.41	12.62	1.63	1.47	6.47	3.77	1.66	0.91	760	Ni-base	[17,25]

Table 3
Information of LPT phase used in CALPHAD calculation.

Planar defects	Symbol	Pearson symbol	Space group	Space number	Strukturbericht designation	Prototype	Stacking sequence on close-packed plane	Description	Ordering of solute elements	Used phase data in TCNI11
-	γ	cF4	$Fm\bar{3}m$	225	$A1$	Cu	ABC	FCC	Disordered	DIS_FCC_A1
-	γ'	cP4	$Pm\bar{3}m$	221	$L1_2$	Cu_3Au	ABC	Ordered FCC	Ordered	FCC_L12
SISF	ε	hP2	$P6_3/mmc$	194	$A3$	Mg	AB	HCP	Disordered	HCP_A3
SESF	ε'	hP4			$A3'$	Nd	ABAC	Doubled HCP (DHCP)		HCP_A3
SISF	χ	hP8			$D0_{19}$	Co_3W	AB	Ordered HCP	Ordered	TIAL3_D019
SESF	η	hP16			$D0_{24}$	Ni_3Ti	ABAC	Ordered DHCP		NI3TI_D024

Table 4
Summary for LPT phase at SISF.

Alloys	SISE energy based on ε LPT phase /mJ·m^{-2}	SISE energy based on χ LPT phase /mJ·m^{-2}	Preferentially formed LPT phase	Reported LPT phase	Judge.	Ref.
2Ta	309.7	165.6	χ	χ	○	[9]
CrTa	243.5	144.6	χ	χ	○	[9]
6Ti	625.4	503.5	χ	χ	○	[9]
ERBOCo−2Ta	247.1	178.2	χ	χ	○	[28]
CoNi-A	903.2	976.4	ε	χ	×	[12]
CoNi-C	963.8	1129.4	ε	χ	×	[9]
ERBOCo−1	1237.3	1336.8	ε	χ	×	[26]
MD2	2330.8	2384.4	ε	No-data	-	[15]
RRHT3	1864.9	1929.0	ε	χ	×	[24]
RRHT5	1748.9	1767.5	ε	χ	×	[24]
ME3	1977.1	2006.0	ε	γ	○	[3]
ME501	1957.2	1928.6	χ	χ	○	[16]
LSHR	1973.7	1866.1	χ	χ	○	[3]
TSNA−1	1934.5	1838.3	χ	χ	○	[17,25]

calculation using phase data only with a state of “enter”. Therefore, the LPT phases can be regarded as a metastable phase that needs additional energy to form. Basically, the concept of this calculation approach corresponds to “parallel tangent construction” approach to estimate the segregation isotherm around grain boundary [39]. The temperatures in the calculation were the same as those in the previous experimental research. Furthermore, 1 standard atmospheric pressure was assumed. Notably, this approach predicts LPT phase and solute partition at stacking fault under thermal equilibrium conditions.

Table 5
Solute partition between LPT phase at SISF and γ′ phase. "P" indicates "positive partition", that the solute is more distributed to the LPT phase, while "N" indicates "negative partition", that the solute is less distributed to the LPT phase. "E" indicates "equal partition", that the solute is almost equally distributed between the LPT phase and γ′ phase. Back colors in orange, blue, and green indicate positive, negative, and equal partition, respectively. "n.d." indicates that there is no information in previous research. The number in the calculation column indicates the partitioning rate defined by Eq. (4). ○ in the column of "Judge." indicates that the preferentially partition phase of the element is coincident between experiment and calculation, "△" indicates that calculated result cannot be judged due to equal experimental partition, and "×" indicates that preferentially partition phase of the element is opposite between experiment and calculation.

Alloys		Partition between LPT phase and γ′ phase $k_i = c_i^{LPT}/c_i^{\gamma'}$									Assumed LPT phase	Ref.
		Ni	Co	Cr	Mo	W	Al	Ti	Ta	Nb		
2Ta	Cal.	-	0.96	-	-	1.73	0.07	-	2.89	-	χ	[9]
	Exp.	-	N	-	-	P	N	-	P	-	χ	
	Judge.	-	○	-	-	○	○		○	-	○	
CrTa	Cal.	-	0.99	0.33	-	1.62	0.07	-	3.69	-	χ	[9]
	Exp.	-	E	E	-	P	N	-	P	-	χ	
	Judge.	-	△	△	-	○	○	-	○	-	○	
6Ti	Cal.	-	0.95	-	-	2.81	0.34	0.0001	-	-	χ	[9]
	Exp.	-	E	-	-	P	N	E	-	-	χ	
	Judge.	-	△	-	-	○	○	△	-	-	○	
ERBOCo-2Ta	Cal.	-	0.96	-	-	1.72	0.09	-	3.02	-	χ	[28]
	Exp.	-	N	-	-	P	N	-	P	-	χ	
	Judge.	-	○	-	-	○	○	-	○	-	○	
MD2	Cal.	0.52	10.90	6.79	10.02	0.32	0.002	0.0004	0.07	-	ε	[15]
	Exp.	N	P	P	n.d.	n.d.	N	n.d.	n.d.	n.d.	n.d.	
	Judge.	○	○	○	-	-	○	-	-	-	-	
ME3	Cal.	0.17	4.51	33.68	6.13	0.25	0.00001	0.0001	0.02	0.01	ε	[3]
	Exp.	N	P	P	P	E	N	E	E	N	γ	
	Judge.	○	○	○	○	△	○	△	△	○	○	
ME501	Cal.	0.20	8.24	25.29	115.28	121.50	0.00001	0.0002	0.01	0.01	χ	[16]
	Exp.	N	P	P	P	P	N	n.d.	n.d.	n.d.	χ	
	Judge.	○	○	○	○	○	○	-	-	-	○	
LSHR	Cal.	0.31	4.03	13.10	21.12	89.26	0.00006	0.0005	0.02	0.02	χ	[3]
	Exp.	N	P	P	P	P	N	N	E	P	χ	
	Judge.	○	○	○	○	○	○	○	△	×	○	
TSNA-1	Cal.	0.32	7.94	13.35	64.83	160.10	0.00006	0.0006	0.01	0.03	χ	[17,25]
	Exp.	N	P	n.d.	P	n.d.	N	n.d.	n.d.	n.d.	χ	
	Judge.	○	○	-	○	-	○	-	-	-	○	

3. Results and discussions

3.1. LPT phase at SISF

First, the prediction of LPT phase at SISF was conducted. Fig. 2 shows calculated SISF energy after the event of Suzuki effect based on Eq. (1) using the LPT phases of ε and χ phases. Each class of superalloys shows a clear difference in tendency in SISF energy. In the case of Co-base superalloys, SISF energy to form χ LPT phase in 2Ta, CrTa, 6Ti, and ERBOCo-2Ta is 165.6, 144.6, 503.5, and 178.2 mJ/m^2 that is lower than those to form ε phase in each alloy. While in the case of CoNi-base superalloys, SISF energy to form ε LPT phase is 903.2, 963.8, and 1237.3 mJ/m^2 in CoNi-A, CoNi-C, and ERBOCo-1 that is lower than those to form χ LPT phase. Different from Co-base and CoNi-base superalloys, the preferentially formed LPT phase is competitive in the case of Ni-base superalloys. MD2, RRHT3, RRHT5, and ME3 show lower SISF energy to form ε LPT phase 2330.8, 1864.9, 1748.9, and 1977.1 mJ/m^2 than those to form χ LPT phase, however, ME501, LSHR, and TSNA-1 shows lower SISF energy to form χ LPT phase than ε phase, 1928.6, 1866.1, and 1838.3 mJ/m^2, respectively. Table 4 summarizes the preferentially formed LPT phase based on the above calculations and referenced LPT phase in previous research. Except for MD2 and ME3, most of LPT phase has been reported to be χ phase in previous research. Notably, the observed γ phase at SISF in ME3 can be recognized as ε phase with disorder atomic arrangement, therefore, this calculation also reproduces the LPT phase at SISF in ME3. However, some alloys such as CoNi-A, CoNi-C, ERBOCo-1, RRHT3, and RRHT5 show that the preferentially formed LPT phase is ε phase which is different from the previous report. Except for CoNi-base superalloys and some of Ni-base superalloys mentioned above RRHT3 and RRHT5, CALPHAD approach in this research shows good agreement with the preferentially formed LPT phase as reported in previous research. This implies that LPT phase at SISF in the above alloys might not have completely ordered or disordered atomic arrangement in previous experimental research as a scenario.

3.2. Solute partition between SISF and γ′ precipitates

Table 5 summarizes the solute partition between LPT phase at SISF and γ′ phase calculated by CALPHAD approach based on the preferentially formed LPT phase at SISF listed in Table 5 with a comparison of previous research. Notably, "equal partition" observed in previous experiments is not evaluated because CALPHAD approach does not predict equal partition. The solute partition is calculated using Eq. (4), where c_i^{LPT} is the composition of the i-th element in LPT phase and $c_i^{\gamma'}$ is that in γ′ phase. In this comparison, the data of CoNi-A, CoNi-C, ERBOCo-1, RRHT3, and RRHT5 were ruled out because CALPHAD approach in the previous section did not reproduce the atomic ordering of LPT phase reported in previous research.

$$k_i = c_i^{LPT}/c_i^{\gamma'} \tag{4}$$

According to Table 5, calculated partitions of main elements such as Ni, Co, Cr, and Al reproduce experimental partition. In the case of γ

Table 6
Partition between bulk χ phase and γ' phase. The phase surrounded by parentheses in a column of the system indicates that the phase is calculated to be metastable, zero volume fraction [40-42].

Alloy	Method	Temperature °C	System	Partition between bulk LPT phase and γ' phase $k_i = c_i^{LPT}/c_i^{\gamma'}$ Ni	Co	W	Al	Ti	Nb	Ta	Ref.
Co-Al-W	Cal.	900	$\gamma+\gamma+\chi$		0.96	2.30	0.24				
	Exp.		$\gamma+\gamma+\chi$		0.96	1.76	0.27				[40]
	Judge.				○	○	○				
Co-Al-W-Ti	Cal.	900	$\gamma+\gamma+\chi$		0.95	2.65	0.33	0.0001			
	Exp.		$\gamma+\gamma+\chi$		0.97	1.52	0.37	1.21			[40]
	Judge.				○	○	○	×			
Co-Al-W-Ni	Cal.	900	$\gamma+\gamma+\chi$	0.20	0.98	2.26	0.24				
	Exp.		$\gamma+\gamma+\chi$	0.57	0.98	1.78	0.23				[40]
	Judge.			○	○	○	○				
Co-Al-W-10Ni	Cal.	900	$\gamma+\gamma+(\chi)$	0.27	1.05	2.19	0.20				
	Exp.		$\gamma+\gamma+\chi$	0.62	1.04	1.88	0.15				[41]
	Judge.			○	○	○	○				
Co-Al-W-20Ni	Cal.	900	$\gamma+\gamma+(\chi)$	0.35	1.14	2.33	0.12				
	Exp.		$\gamma+\gamma+\chi$	0.64	1.09	1.86	0.31				[41]
	Judge.			○	○	○	○				
Co-Al-W-30Ni	Cal.	900	$\gamma+\gamma+(\chi)$	0.45	1.25	2.41	0.04				
	Exp.		$\gamma+\gamma+\chi$	0.55	1.27	2.06	0.17				[41]
	Judge.			○	○	○	○				
Co-Al-W-40Ni	Cal.	900	$\gamma+\gamma+(\chi)$	0.53	1.41	2.52	0.01				
	Exp.		$\gamma+\gamma+\chi$	0.58	1.41	2.11	0.17				[41]
	Judge.			○	○	○	○				
Co-Al-W-Nb	Cal.	850	$\gamma+\gamma+\chi$		0.97	2.46	0.23		0.001		
	Exp.		$\gamma+\gamma+\chi$		0.97	1.59	0.30		1.93		[42]
	Judge.				○	○	○		×		
Co-Al-W-Ta	Cal.	900	$\gamma+\gamma+\chi$		0.95	2.91	0.14			1.99	
	Exp.		$\gamma+\gamma+\chi$		0.96	1.68	0.31			1.81	[42]
	Judge.				○	○	○			○	

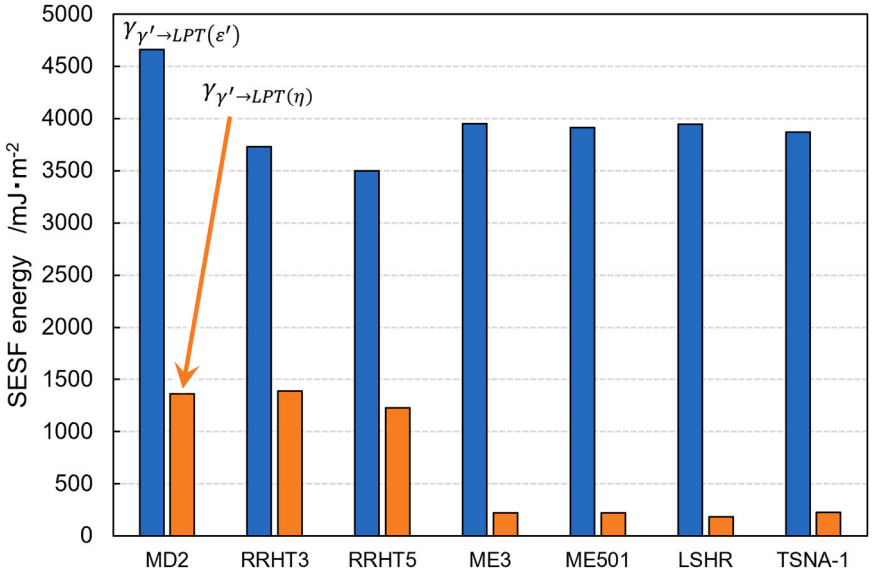

Fig. 3. SESF energy to form LPT phase in γ' precipitates after the event of Suzuki effect.

Table 7
Summary for LPT phase at SESF.

Alloys	SESF energy based on ε' LPT phase /mJ·m^{-2}	SESF energy based on η LPT phase /mJ·m^{-2}	Preferentially formed LPT phase	Reported LPT phase	Judge.	Ref.
MD2	4661.7	1361.7	η	No-data	-	[15]
RRHT3	3729.8	1389.9	η	η	○	[24, 38]
RRHT5	3497.8	1226.6	η	γ	×	[24, 38]
ME3	3954.3	220.2	η	γ	×	[3]
ME501	3914.3	223.9	η	η	○	[16]
LSHR	3947.4	184.6	η	η	○	[3]
TSNA−1	3869.0	228.2	η	η	○	[17, 25]

former heavy elements such as Mo and W, the partition is also reproduced. In the case of γ′ former elements such as Ti, Ta, and Nb, it is difficult to judge whether the calculated solute partition is correct or not because equal partition is frequently reported in previous experimental research. However, the solute partition of Ta in Co-base superalloys such as 2Ta, CrTa, 6Ti, and ERBOCo-2Ta reproduces the positive partition by calculation. On the other hand, the solute partition of Nb is always calculated to be a negative partition even in the alloys with positive partition reported in previous experimental research such as LSHR. This discrepancy in Nb partition could originate from the accuracy of the database used in this research.

3.3. Solute partition between bulk LPT phase and γ′ phase

To evaluate the accuracy of the database used in this manuscript, the solute partition between bulk LPT phase based on SISF and γ′ phase is calculated using CALPHAD approach in the alloy system with γ, γ′, and bulk χ phase which has been already reported experimentally. In this calculation, γ, γ', and χ phases are treated as "enter" phases. Table 6 summarizes the comparison of the calculated solute partition between bulk χ phase and γ′ phase with the experimental one. Notably, Table 6 shows only the alloy system with γ, γ′, and bulk χ phases because no previous works using the alloy system with γ, γ′, and bulk ε phases were found. Furthermore, it should be noted that calculated composition of γ and γ′ phases is comparable with experimental ones. Table 6 indicates that calculated solute partition of main elements such as Ni, Co, and Al reproduces the experimental one as well as that of γ former heavy element such as W. In the case of γ′ former element, the calculated solute partition of Ta reproduces the experimental one, however, that of Ti and Nb is negative which is the opposite trend to the experimental one. Therefore, the database of Ti and Nb in χ phase is necessary to be modified to more accurately predict LPT phase.

3.4. Case of SESF

In addition to the case of SISF, the solute partition at SESF was tried to calculate using MD2, RRHT3, RRHT5, ME3, ME501, LSHR, and TSNA-1 within the range of Ni-base superalloys because experimental works focusing on the solute partition at SESF is less reported than those at SISF. Figure 4 shows SESF energy in each alloy. Fig. 3 indicates that SESE energy assuming η phase as an LPT phase is lower than that of ε' phase in all the alloys.

Table 7 summarizes SESF energy. Since SESF energy assuming η phase as an LPT phase is lower than that of ε phase in all the cases,

Table 8
Solute partition between SESF and γ′ precipitates.

Alloys		Partition between LPT phase and γ' phase $k_i = c_i^{LPT}/c_i^{\gamma'}$									Assumed LPT phase	Ref.
		Ni	Co	Cr	Mo	W	Al	Ti	Ta	Nb		
MD2	Cal.	1.05	0.03	0.14	0.002	0.03	0.72	0.48	4.16	-	η	[15]
	Exp.	N	P	P	n.d.	n.d.	N	n.d.	n.d.	-	n.d.	
	Judge.	×	×	×	-	-	○	-	-		-	
ME501	Cal.	1.06	0.05	1.08	0.003	0.36	0.78	0.25	4.41	0.01	η	[16]
	Exp.	N	P	E	P	E	N	P	P	P	η	
	Judge.	×	×	△	×	△	○	×	○	×	○	
LSHR	Cal.	1.14	0.03	0.89	0.001	0.27	0.75	0.28	14.98	0.01	η	[3]
	Exp.	N	P	E	P	P	N	P	P	P	η	
	Judge.	×	×	△	×	×	○	×	○	×	○	
TSNA-1	Cal.	1.07	0.05	1.08	0.003	0.36	0.78	0.25	4.26	0.01	η	[17,25]
	Exp.	N	P	n.d.	n.d.	n.d.	N	P	n.d.	P	η	
	Judge.	×	×	-	-	-	○	×	-	×	○	

Table 9
Composition of modified ME501 for the verification of database (at%) The calculation was conducted at 760 °C.

Alloys	Ni	Co	Cr	Mo	W	Al	Ti	Ta	Nb	$V_{\gamma'}$
ME501	52.50	18.15	13.71	1.80	0.97	6.61	3.72	1.58	0.96	0.48
-no Cr	60.84	21.03	-	2.09	1.12	7.66	4.31	1.83	1.11	0.51
-no Mo	53.46	18.48	13.96	-	0.99	6.73	3.79	1.61	0.98	0.50
-no W	53.01	18.33	13.84	1.82	-	6.67	3.76	1.60	0.97	0.48
-no MoW	54.00	18.67	14.10	-	-	6.80	3.83	1.63	0.99	0.50
-no Ti	54.53	18.85	14.24	1.87	1.01	6.87	-	1.64	1.00	0.28
-no Ta	53.34	18.44	13.93	1.83	0.99	6.72	3.78	-	0.98	0.43
-noNb	53.01	18.33	13.84	1.82	0.98	6.67	3.76	1.60	0.00	0.45
-noTiTa	55.44	19.17	14.48	1.90	1.02	6.98	-	-	1.01	0.29
-no TiNb	55.08	19.04	14.38	1.89	1.02	6.93	-	1.66	-	0.25
-no NbTa	53.87	18.62	14.07	1.85	1.00	6.78	3.82	-	-	0.42
-no TiTaNb	56.01	19.36	14.63	1.92	1.03	7.05	-	-	-	0.28

Table 10
Solute partition between η LPT phase and γ' precipitates using modified ME501 virtual superalloys (at%) The calculation was conducted at 760 °C.

Alloys		Partition between LPT phase and γ' phase $k_i = c_i^{LPT}/c_i^{\gamma'}$									Assumed LPT phase
		Ni	Co	Cr	Mo	W	Al	Ti	Ta	Nb	
ME501	Exp..	N	P	E	P	E	N	P	P	P	η
	Cal.	1.06	0.05	1.08	0.0003	0.36	0.78	0.25	4.41	0.01	η
	Judge.	×	×	△	×	△	○	×	○	×	
-no Cr	Cal.	1.08	0.04	-	0.0002	0.05	0.77	0.25	5.00	0.01	η
	Judge.	×	×		×	△	○	×	○	×	
-no Mo	Cal.	1.06	0.05	0.94	-	0.29	0.78	0.25	4.50	0.01	η
	Judge.	×	×	△		△	○	×	○	×	
-no W	Cal.	1.06	0.05	0.98	0.0003	-	0.78	0.25	4.41	0.01	η
	Judge.	×	×	△	×		○	×	○	×	
-no MoW	Cal.	1.06	0.05	0.83	-	-	0.78	0.25	4.50	0.01	η
	Judge.	×	×	△			○	×	○	×	
-no Ti	Cal.	1.03	0.06	0.39	0.0001	0.08	0.70	-	2.51	0.01	η
	Judge.	×	×	△	×	△	○		○	×	
-no Ta	Cal.	1.05	0.61	0.44	0.48	0.19	0.16	2.29	-	1.62	η
	Judge.	×	×	△	×	△	○	○		○	
-noNb	Cal.	1.06	0.05	0.76	0.0004	0.24	0.74	0.32	3.83	-	η
	Judge.	×	×	△	×	△	○	×	○	-	
-noTiTa	Cal.	0.72	1.87	5.59	1.04	3.42	0.0002	-	-	0.005	η
	Judge.	○	○	△	○	△	○	-	-	×	
-no TiNb	Cal.	1.02	0.07	0.28	0.0001	0.06	0.68	-	2.14	-	η
	Judge.	×	×	△	×	△	○		○		
-no NbTa	Cal.	1.10	0.38	0.22	0.12	0.06	0.25	2.44	-	-	η
	Judge.	×	×	△	×	△	○	○	-	-	
-no TiTaNb	Cal.	0.82	1.68	3.83	0.72	2.57	0.00	-	-	-	η
	Judge.	○	○	△	×	△	○	-	-	-	

Table 11
Partition between bulk η phase and γ' phase. Number in orange indicates a positive partition, and that in blue indicates a negative partition. A name of a phase surrounded by parentheses in a column of the system indicates that the phase is calculated to be metastable [43,44].

Alloy	Method	Temperature °C	System	Partition between bulk LPT phase and γ' phase $k_i = c_i^{LPT}/c_i^{\gamma'}$				
				Ni	Al	Ti	Ta	Ref.
Ni-Al-Ti	Cal.	900	$\gamma + \gamma' + \eta$	0.98	0.32	1.47	-	[43]
	Exp.		$\gamma + \gamma' + \eta$	0.98	0.50	1.30	-	
	Judge.			○	○	○	-	
Ni-Al-Ta	Cal.	1250	$\gamma + (\gamma') + \eta$	0.97	0.85	-	1.48	[44]
	Exp.		$\gamma + \gamma' + \eta$	0.99	0.76	-	1.38	
	Judge.			○	○	-	○	

therefore, preferentially formed LPT phase at SESF among listed Ni-base superalloys are expected to be η phase. In previous experimental research, except for RRHT5 and ME3, LPT phase at SESF is reported to be η phase, which is consistent with this estimation by CALPHAD approach. Because this manuscript regards the observed γ phase at SESF as ε' phase with disorder atomic arrangement, the prediction of LPT phase at SESF in RRHT5 and ME3 by calculation also failed to reproduce the experimental one. As in a similar manner of SISF, this result indicates that the observed atomic ordering of LPT phases in RRHT 5 and ME3 in the previous experiment might not have a completely disordered atomic arrangement.

Based on the expected preferentially formed LPT phase at SESF based on Table 7, the solute partition between LPT phase and γ' phase is calculated using CALPHAD approach shown in Table 8. Notably, the data of RRHT5 and ME3 are excluded from Table 8 because of the incorrect prediction of LPT phase, and the data of RRHT3 is also excluded because of no available experimental data. Different from the case of SISF, the calculated solute partition is quite different from the experimental one. Main elements such as Ni, Co, and Cr, furthermore, γ former heavy elements such as Mo, γ' former elements such as Ti and Nb show different preferentially partition phase in the calculation towards experimental ones. The solute partition of only Al and Ta can always reproduce experimental ones by calculation among all the alloys.

The discrepancy of the solute partition at SESF between calculation and experiment might come from the accuracy of the database in η phase. Since the partition of almost all the elements failed to reproduce the experimental ones even in main elements such as Ni, Co, and Cr, some specified elements of η phase in the database could affect the calculation results. Therefore, as a verification of the database, the solute partition between η LPT phase and γ' precipitates was re-evaluated using virtual superalloys based on ME501 by modifying the nominal composition so that one specified element is removed keeping a ratio of remaining elements. The virtual superalloys used in this verification are listed in Table 9.

The calculated solute partition using the virtual superalloys is shown in Table 10 under the condition that γ and γ' phases are treated as "enter" phase but η phase is treated as "dormant" phase in the calculation. Since the solute partition of main elements especially for Ni, Co, and Al is always observed in experimental research, the reproduction of the solute partition of such elements is the most important issue. Table 10 shows that among all the modified ME501 virtual superalloys, only ME501-noTiTa and ME501-noTiTaNb reproduce the experimental solute partition of main elements such as Ni, Co, Cr, and Al in the calculation. This result indicates that accuracy of database of Ti and Ta in η phase could be low. Notably, the solute partition of heavy elements such as Nb in ME501-noTiTa and Mo in ME501-noTiTaNb failed to reproduce the experimental partition. However, experimental solute partition of Nb was reproduced only in ME501-noTa, and that of Mo was reproduced only in ME501-noTiTa, as shown Table 10. This result also indicates that accuracy of database of Ti and Ta in η phase could be low.

To confirm the accuracy of the database of Ti and Ta in η phase, the solute partition between bulk η phase and γ' precipitates was compared between calculation and experiment in ternary system. The results are shown in Table 11. In the ternary system, the solute partition by the calculation reproduced the experimental one regardless of containing Ti and Ta. Therefore, the problem of reproducing the solute partition can be assumed in the database of physical properties between Ti and Ta in η phase in a multi-component system.

4. Conclusion

1. In the case of SISF, stacking fault energy to form ε LPT phase and that of χ LPT phase is competed with each other in Ni-base superalloys. Co-base superalloys and Ni-base superalloys such as ME501, LSHR, and TSNA-1 are predicted to preferentially form χ LPT phase at SISF.
2. Calculated solute partition between χ LPT phase and γ' phase reproduced experimental solute partition between SISF and γ' phase especially in main elements such as Ni, Co, Cr, and Al, moreover, γ former heavy elements such as Mo and W. However, the calculated partition of γ' former elements such as Ti and Nb showed opposite preferentially distributed phases in the comparison with the experimental one. Database of physical properties of Ti and Nb in χ phase could have lower accuracy.
3. In the case of SESF, all the alloys in the calculation are predicted to form η LPT phase at SESF. However, the calculated solute partition between η and γ' phases of almost all the elements except for Al and Ta did not reproduce the experimental tendency of preferentially distributed phases of elements. This discrepancy comes from the inadequate accuracy of the database of physical properties in η phase with a multi-component system between Ti and Ta in the calculation.

CRediT authorship contribution statement

Takuma Saito: Formal analysis, Investigation, Methodology, Writing – original draft, Data curation. **Hiroshi Harada**: Conceptualization, Supervision, Writing – review & editing. **Taichi Abe**: Writing – review & editing. **Hideyuki Murakami**: Writing – review & editing.

Declaration of Competing Interest

The authors declare that they have no known competing financial interests or personal relationships that could have appeared to influence the work reported in this paper.

Acknowledgement

The authors would like to appreciate Dr. Makoto Osawa at NIMS for a discussion about a basic concept of this work, Dr. Toshio Osada, Dr. Ayako Ikeda, and Dr. Kyoko Kawagishi for support of CALPHAD simulators.

Appendix A. Detailed picture of crystal structure and ordering in γ′ and LPT phases

Fig. A1 shows crystal structures of based on Ni_3Al. Fig. A1 (a) shows the unit-cell of γ′ phase. Since the slip plane of superalloys at intermediate temperature such around 800 °C is {111}, Fig. A1 (b) shows the atomic stacking of γ′ phase on (111). Notably, Fig. A1 (b) is not an unit-cell of γ′ phase. Via dislocation motion, planaer defects such as stacking fault form in γ′ phase. Fig. A1 (c) shows the superlattice intrinsic stacking fault (SISF) in γ′ phase, and Fig. A1 (d) shows the superlattice extrinsic stacking fault (SESF) in γ′ phase.

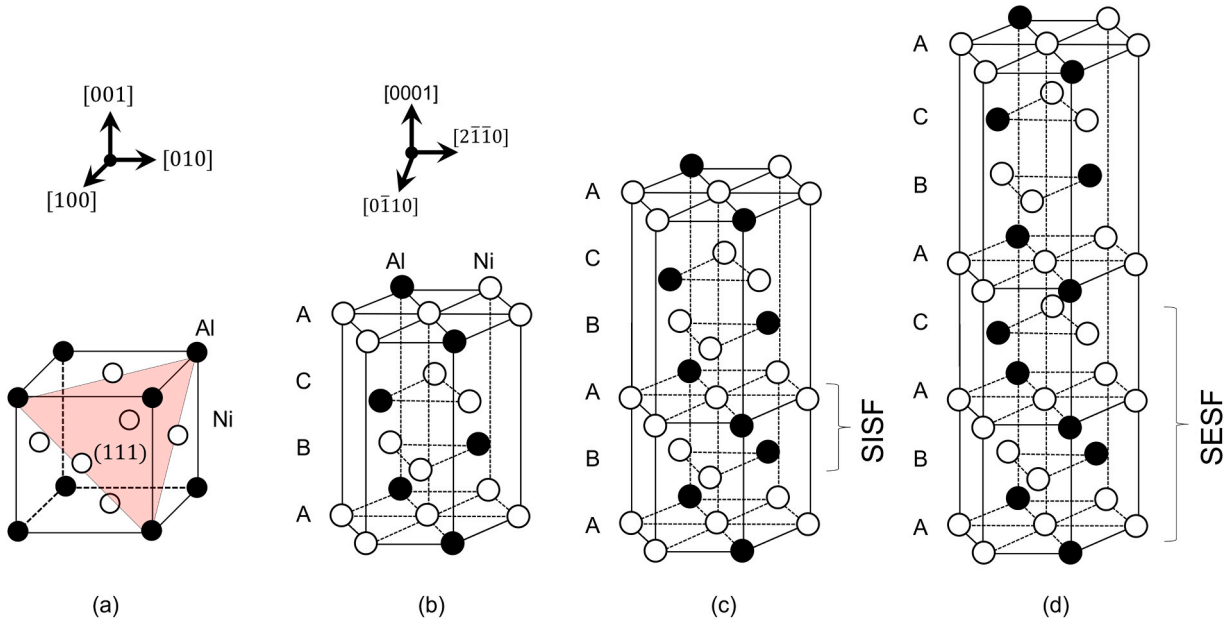

Fig. A1. Crystal structure of γ′ phase based on Ni_3Al. (a) Unit-cell of γ′ phase, (b) atomic stacking of γ′ phase on (111), (c) SISF in γ′ phase, (d) SESF in γ′ phase.

SISF and SESF in γ′ phase can be approximated as LPT phases. Fig. A2 shows the crystal structure of LPT phases, based on Table 3. Atomic stacking in SISF shown in Fig. A1 (c) is identical to that of χ and ε phases in Fig. A2 (a, b), and that in SESF shown in Fig. A1 (d) is identical to that of η and ε' phases in Figs. A2 (c, d), except for the solute ordering.

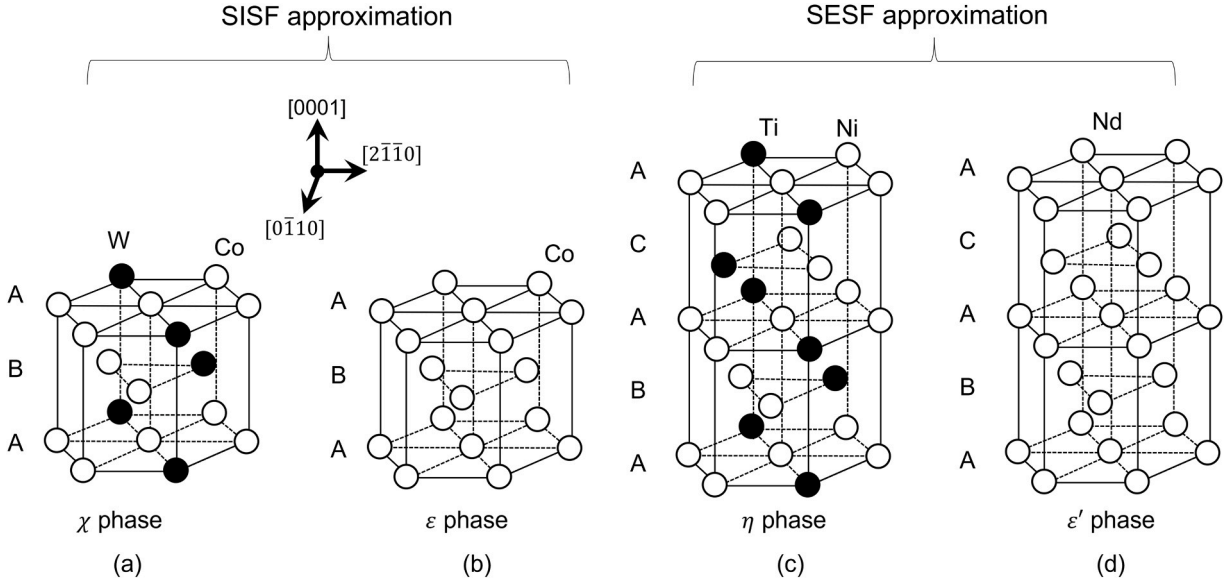

Fig. A2. Crystal structure of LPT phases. (a) Unit-cell of χ phase based on Co_3W, (b) unit-cell of ε phase based on Co, (c) unit-cell of η phase, (d) unit-cell of ε' phase based on Nd.

To calculate the stacking fault energy defined by Eq. (1), atomic plane at stacking fault, n, has to be estimated. Fig. A3 shoes how to estimate n value including x and m values by assuming a motion of zonal $\frac{1}{3}a < 11\bar{2} >$ dislocation, more visualizely. Notably, zonal dislocation is usually termed as a

group of dislocations among several atomic planes, as if it was one individual dislocation.

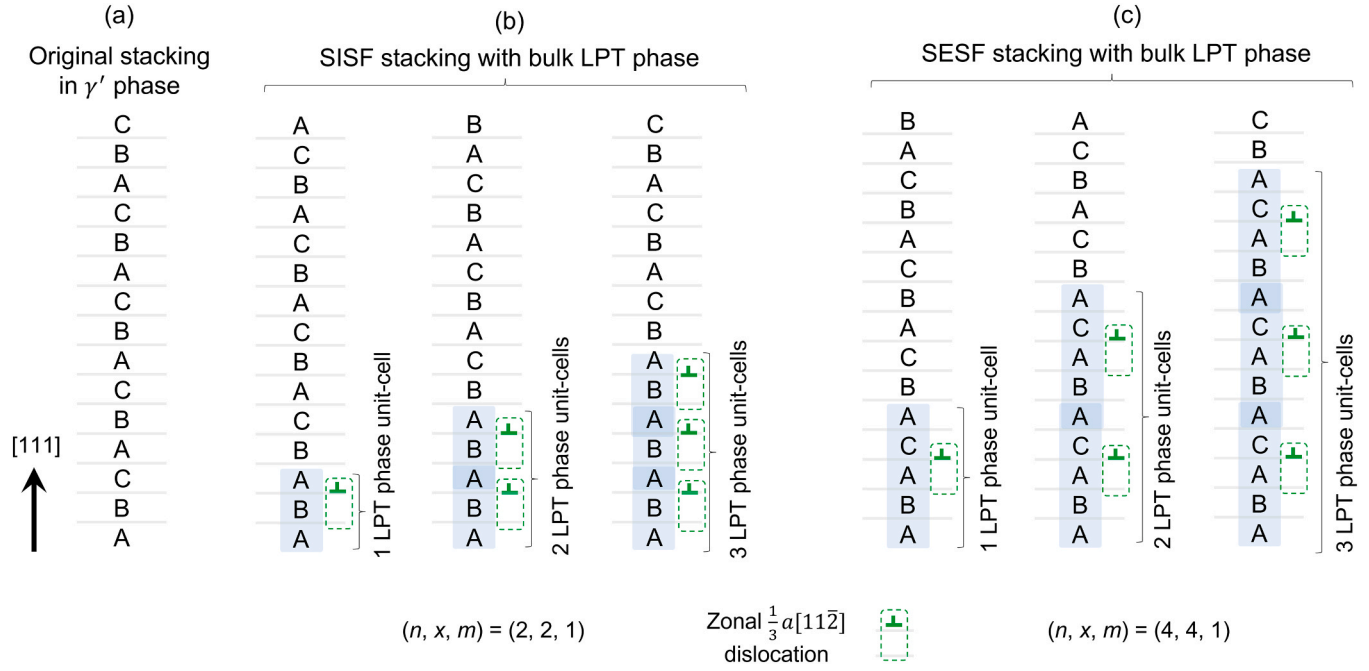

Fig. A3. Estimating atomic plane n to calculate stacking fault energy.

The formation mechanism and their detailed atomic arrangment in γ′ phase are shown in Fig. A4, based on previous articles [35,45]. If the perfect dislocation $\frac{1}{2}a[10\bar{1}]$ consisting of two Shockley partials such as $\frac{1}{6}a[11\bar{2}]$ and $\frac{1}{6}a[2\bar{1}\bar{1}]$ move on the same slip plane (111), Al-Al nearest neighbor bond emerges between Al atoms in neighboring slip planes in APB. And APB is characterized by Al-Al nearest neighbor bond, resulting in higher fault energy than any other planer faults [46]. APB usually has small width between perfect dislocations because of its high falut energy. Regarding superlattice stacking fault, zonal $\frac{1}{3}a[11\bar{2}]$ forms Al-Al nearest neighbor bond in two-layers at first called complex intrinsic stacking fault (CISF) or complex extrinsic stacking fault (CESF), and then, Al-Al nerest neighbor bond can be removed by re-ordering atoms between two-layers, finaly, SISF and SESF forms.

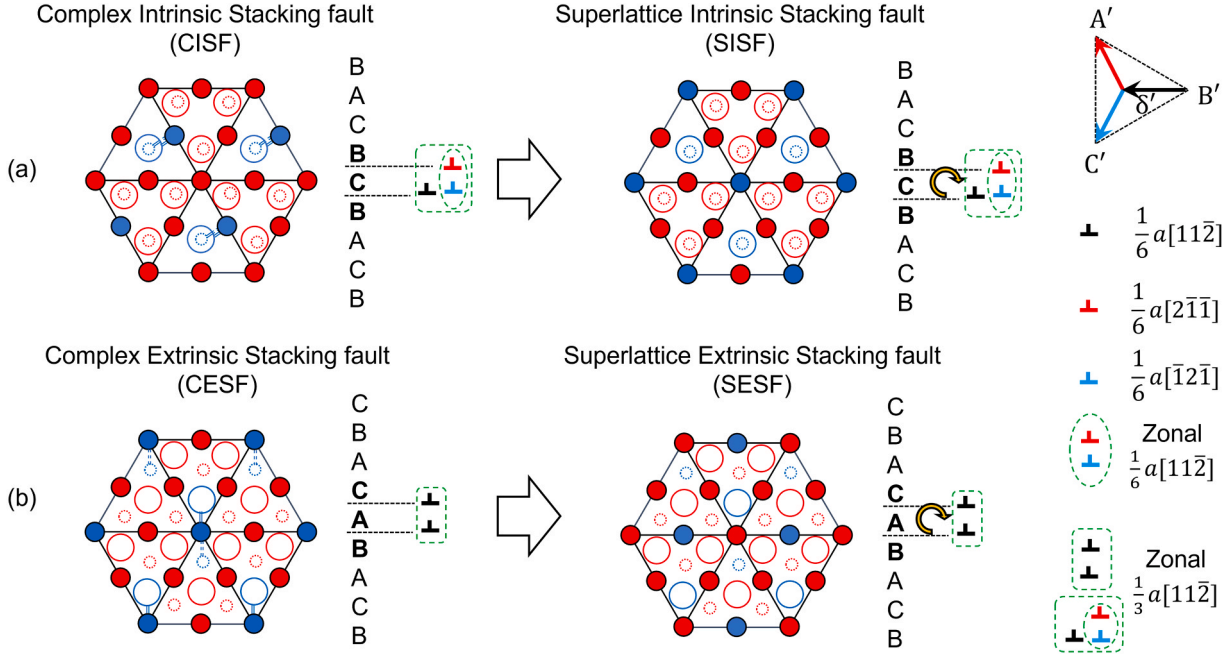

Fig. A4. Atomic stacking and the formation mechanism of planar faults in γ′ phase. (a) Perfect crystal of γ′ phase based on Ni_3Al, (b) APB, (c) formation mechanism of SISF, (d) formation mechanism of SESF. Letters of the atomic layers in bold show equivalent layeys in correspoding figures.

References

[1] C.M.F. Rae, R.C. Reed, Primary creep in single crystal superalloys: Origins, mechanisms and effects, Acta Mater. 55 (2007) 1067–1081, https://doi.org/10.1016/j.actamat.2006.09.026.

[2] T. Smith, B. Esser, N. Antolin, A. Carlsson, R. Williams, A. Wessman, T. Hanlon, H. Fraser, W. Windl, D. McComb, Phase transformation strengthening of high-temperature superalloys, Nat. Commun. 7 (2016) 13434, https://doi.org/10.1038/ncomms13434.

[3] T.M. Smith, B.S. Good, T.P. Gabb, B.D. Esser, A.J. Egan, L. Evans, D. McComb, M. Mills, Effect of stacking fault segregation and local phase transformations on creep strength in Ni-base superalloys, Acta Mater. 172 (2019) 55–65, https://doi.org/10.1016/j.actamat.2019.04.038.

[4] H. Suzuki, Chemical interaction of solute atoms with dislocations, Rep. Res. Inst. Tohoku Univ. 4 (1952) 455–463.

[5] R. Heidenreich, W. Schockley, Study of slip in aluminum crystals by electron microscope and electron diffraction methods. Report of a Conference on the Strength of Solids, Physical Society, London, 1948, pp. 67–75.

[6] H. Suzuki, The yield strength of binary alloys. Dislocations and Mechanical Properties of Crystals, John Wiley and Sons, New York, 1957, pp. 361–390.

[7] A.J. Egan, Y. Rao, G.B. Viswanathan, T.M. Smith, M. Ghazisaeidi, S. Tin, M.J. Mills, Effect of Nb alloying addition on local phase transformation at microtwin boundaries in nickel-based superalloys. Proceedings of the 14th International Symposium on Superalloys, Springer, Seven Springs Mountain Resort, 2020, pp. 640–650, https://doi.org/10.1007/978-3-030-51834-9_62.

[8] M.S. Titus, R.K. Rhein, P.B. Wells, P.C. Dodge, G.B. Viswanathan, M.J. Mills, A. Van der Ven, T.M. Pollock, Solute segregation and deviation from bulk thermodynamics at nanoscale crystalline defects, Sci. Adv. 2 (2016) e1601796, https://doi.org/10.1126/sciadv.1601796.

[9] M.S. Titus, A. Mottura, G.B. Viswanathan, A. Suzuki, M.J. Mills, T.M. Pollock, High resolution energy dispersive spectroscopy mapping of planar defects in $L1_2$-containing Co-base superalloys, Acta Mater. 89 (2015) 423–437, https://doi.org/10.1016/j.actamat.2015.01.050.

[10] G.B. Viswanathan, R. Shi, A. Genc, V.A. Vorontsov, L. Kovarik, C.M.F. Rae, M. J. Mills, Segregation at stacking faults within the γ' phase of two Ni-base superalloys following intermediate temperature creep, Scr. Mater. 94 (2015) 5–8, https://doi.org/10.1016/j.scriptamat.2014.06.032.

[11] T. Smith, B. Esser, N. Antolin, G. Viswanathan, T. Hanlon, A. Wessman, D. Mourer, W. Windl, D. McComb, M. Mills, Segregation and η phase formation along stacking faults during creep at intermediate temperatures in a Ni-based superalloy, Acta Mater. 100 (2015) 19–31, https://doi.org/10.1016/j.actamat.2015.08.053.

[12] Y.M. Eggeler, J. Müller, M.S. Titus, A. Suzuki, T.M. Pollock, E. Spiecker, Planar defect formation in the γ' phase during high temperature creep in single crystal CoNi-base superalloys, Acta Mater. 113 (2016) 335–349, https://doi.org/10.1016/j.actamat.2016.03.077.

[13] L.P. Freund, O.M. Messé, J.S. Barnard, M. Göken, S. Neumeier, C.M.F. Rae, Segregation assisted microtwinning during creep of a polycrystalline $L1_2$-hardened Co-base superalloy, Acta Mater. 123 (2017) 295–304, https://doi.org/10.1016/j.actamat.2016.10.048.

[14] T.M. Smith, Y. Rao, Y. Wang, M. Ghazisaeidi, M.J. Mills, Diffusion processes during creep at intermediate temperatures in a Ni-based superalloy, Acta Mater. 141 (2017) 261–272, https://doi.org/10.1016/j.actamat.2017.09.027.

[15] D. Barba, T. Smith, J. Miao, M. Mills, R. Reed, Segregation-assisted plasticity in Ni-based superalloys, Metall. Mater. Trans. A 49 (2018) 4173–4185, https://doi.org/10.1007/s11661-018-4567-6.

[16] T.M. Smith, B.D. Esser, B. Good, M.S. Titus, G.B. Viswanathan, C. Rae, M. Ghazisaeidi, D. McComb, M. Mills, Segregation and phase transformations along superlattice intrinsic stacking faults in Ni-based superalloys, Metall. Mater. Trans. A 49 (2018) 4186–4198, https://doi.org/10.1007/s11661-018-4701-5.

[17] T.M. Smith, T.P. Gabb, K.N. Wertz, J. Stuckner, L.J. Evans, A.J. Egan, M.J. Mills, Enhancing the creep strength of next-generation disk superalloys via local phase transformation strengthening. Proceedings of the 14th International Symposium on Superalloys, Springer, Seven Springs Mountain Resort, 2020, pp. 726–736, https://doi.org/10.1007/978-3-030-51834-9_70.

[18] M. Lenz, M. Wu, J. He, S.K. Makineni, B. Gault, D. Raabe, S. Neumeier, E. Spiecker, Atomic Structure and Chemical Composition of Planar Fault Structures in Co-Base Superalloys. Proceedings of the 14th International Symposium on Superalloys, Springer, Seven Springs Mountain Resort, 2020, pp. 920–928, https://doi.org/10.1007/978-3-030-51834-9_90.

[19] X. Wu, S.K. Makineni, C.H. Liebscher, G. Dehm, J.R. Mianroodi, P. Shanthraj, B. Svendsen, D. Bürger, G. Eggeler, D. Raabe, Unveiling the Re effect in Ni-based single crystal superalloys, Nat. Commun. 11 (2020) 389, https://doi.org/10.1038/s41467-019-14062-9.

[20] S. Lu, S. Antonov, L. Li, C. Liu, X. Zhang, Y. Zheng, H.L. Fraser, Q. Feng, Atomic structure and elemental segregation behavior of creep defects in a Co-Al-W-based single crystal superalloys under high temperature and low stress, Acta Mater. 190 (2020) 16–28, https://doi.org/10.1016/j.actamat.2020.03.015.

[21] M. Lenz, M. Wu, E. Spiecker, Segregation-assisted climb of Frank partial dislocations: An alternative route to superintrinsic stacking faults in $L1_2$-hardened superalloys, Acta Mater. 191 (2020) 270–279, https://doi.org/10.1016/j.actamat.2020.03.056.

[22] S. Lu, S. Antonov, F. Xue, L. Li, Q. Feng, Segregation-assisted phase transformation and anti-phase boundary formation during creep of a γ'-strengthened Co-based superalloy at high temperatures, Acta Mater. 215 (2021) 117099, https://doi.org/10.1016/j.actamat.2021.117099.

[23] D. Barba, A.J. Egan, Y. Gong, M.J. Mills, R.C. Reed, Rationalisation of the Micromechanisms Behind the High-Temperature Strength Limit in Single-Crystal Nickel-Based Superalloys. Proceedings of the 14th International Symposium on Superalloys, Springer, Seven Springs Mountain Resort, 2020, pp. 260–272, https://doi.org/10.1007/978-3-030-51834-9_25.

[24] L. Lilensten, S. Antonov, B. Gault, S. Tin, P. Kontis, Enhanced creep performance in a polycrystalline superalloy driven by atomic-scale phase transformation along planar faults, Acta Mater. 202 (2021) 232–242, https://doi.org/10.1016/j.actamat.2020.10.062.

[25] T.M. Smith, N.A. Zarkevich, A.J. Egan, J. Stuckner, T.P. Gabb, J.W. Lawson, M. J. Mills, Utilizing local phase transformation strengthening for nickel-base superalloys, Commun. Mater. 2 (2021) 1–9, https://doi.org/10.1038/s43246-021-00210-6.

[26] S.K. Makineni, A. Kumar, M. Lenz, P. Kontis, T. Meiners, C. Zenk, S. Zaefferer, G. Eggeler, S. Neumeier, E. Spiecker, On the diffusive phase transformation mechanism assisted by extended dislocations during creep of a single crystal CoNi-based superalloy, Acta Mater. 155 (2018) 362–371, https://doi.org/10.1016/j.actamat.2018.05.074.

[27] S.K. Makineni, M. Lenz, S. Neumeier, E. Spiecker, D. Raabe, B. Gault, Elemental segregation to antiphase boundaries in a crept CoNi-based single crystal superalloy, Scr. Mater. 157 (2018) 62–66, https://doi.org/10.1016/j.scriptamat.2018.07.042.

[28] N. Volz, F. Xue, C.H. Zenk, A. Bezold, S. Gabel, A.P.A. Subramanyam, R. Drautz, T. Hammerschmidt, S.K. Makineni, B. Gault, Understanding creep of a single-crystalline Co-Al-W-Ta superalloy by studying the deformation mechanism, segregation tendency and stacking fault energy, Acta Mater. 214 (2021) 117019, https://doi.org/10.1016/j.actamat.2021.117019.

[29] Y. Rao, T.M. Smith, M.J. Mills, M. Ghazisaeidi, Segregation of alloying elements to planar faults in γ'-Ni_3Al, Acta Mater. 148 (2018) 173–184, https://doi.org/10.1016/j.actamat.2018.01.055.

[30] K.V. Vamsi, S. Karthikeyan, High-throughput estimation of planar fault energies in A3B compounds with $L1_2$ structure, Acta Mater. 145 (2018) 532–542, https://doi.org/10.1016/j.actamat.2017.10.029.

[31] L. Feng, Y. Rao, M. Ghazisaeidi, M.J. Mills, Y. Wang, Quantitative prediction of Suzuki segregation at stacking faults of the γ'phase in Ni-base superalloys, Acta Mater. 200 (2020) 223–235, https://doi.org/10.1016/j.actamat.2020.08.056.

[32] M. Egami, I. Ohnuma, M. Enoki, H. Ohtani, E. Abe, Thermodynamic origin of solute-enriched stacking-fault in dilute Mg-Zn-Y alloys, Mater. Des. 188 (2020) 108452, https://doi.org/10.1016/j.matdes.2019.108452.

[33] L. Feng, A. Egan, F. Xue, E. Marquis, M.J. Mills, Y. Wang, Dynamic localized phase transformation at stacking faults during creep deformation and new criterion for superalloy design, MRS Commun. 12 (2022) 991–1001, https://doi.org/10.1557/s43579-022-00251-z.

[34] L. Feng, S.B. Kannan, A. Egan, T. Smith, M.J. Mills, M. Ghazisaeidi, Y. Wang, Localized phase transformation at stacking faults and mechanism-based alloy design, Acta Mater. 240 (2022) 118287, https://doi.org/10.1016/j.actamat.2022.118287.

[35] L. Kovarik, R.R. Unocic, J. Li, P. Sarosi, C. Shen, Y. Wang, M.J. Mills, Microtwinning and other shearing mechanisms at intermediate temperatures in Ni-based superalloys, Prog. Mater. Sci. 54 (2009) 839–873, https://doi.org/10.1016/j.pmatsci.2009.03.010.

[36] G.B. Olson, M. Cohen, A general mechanism of martensitic nucleation: Part I. General concepts and the FCC → HCP transformation, Metall. Trans. A 7 (1976) 1897–1904, https://doi.org/10.1007/BF02659822.

[37] N. Volz, C.H. Zenk, N. Karpstein, M. Lenz, E. Spiecker, M. Göken, S. Neumeier, Creep properties and deformation mechanisms of single-crystalline γ'-strengthened superalloys in dependence of the Co/Ni ratio, Philos. Mag. 102 (2022) 718–744, https://doi.org/10.1080/14786435.2021.2017051.

[38] A.J. Egan, F. Xue, Y. Rao, G. Sparks, E. Marquis, M. Ghazisaeidi, S. Tin, M.J. Mills, Local Phase Transformation Strengthening at Microtwin Boundaries in Nickel-Based Superalloys, Acta Mater. 238 (2022) 118206, https://doi.org/10.1016/j.actamat.2022.118206.

[39] M. Hillert, Phase equilibria, phase diagrams and phase transformations: their thermodynamic basis, Cambridge university press, 2007.

[40] T. Omori, K. Oikawa, J. Sato, I. Ohnuma, U.R. Kattner, R. Kainuma, K. Ishida, Partition behavior of alloying elements and phase transformation temperatures in Co–Al–W-base quaternary systems, Intermetallics 32 (2013) 274–283, https://doi.org/10.1016/j.intermet.2012.07.033.

[41] K. Shinagawa, T. Omori, J. Sato, K. Oikawa, I. Ohnuma, R. Kainuma, K. Ishida, Phase equilibria and microstructure on γ' phase in Co-Ni-Al-W system, Mater. Trans. 49 (2008) 1474–1479, https://doi.org/10.2320/matertrans.MER2008073.

[42] L. Wang, M. Oehring, U. Lorenz, J. Yang, F. Pyczak, Influence of alloying additions on $L1_2$ decomposition in γ-γ' Co-9Al-9W–2X quaternary alloys, Scr. Mater. 154 (2018) 176–181, https://doi.org/10.1016/j.scriptamat.2018.05.051.

[43] P. Nash, W.W. Liang, Phase equilibria in the Ni-Al-Ti system at 1173 k, Metall. Trans. A 16 (1985) 319–322, https://doi.org/10.1007/BF02814329.

[44] P. Willemin, O. Dugue, M. Durand-Charre, J.H. Davidson, Experimental determination of nickel-rich corner of Ni–Al–Ta phase diagram, Mater. Sci. Technol. 2 (1986) 344–348, https://doi.org/10.1179/mst.1986.2.4.344.

[45] V.A. Vorontsov, L. Kovarik, M.J. Mills, C.M.F. Rae, High-resolution electron microscopy of dislocation ribbons in a CMSX-4 superalloy single crystal, Acta Mater. 60 (2012) 4866–4878, https://doi.org/10.1016/j.actamat.2012.05.014.

[46] V. Vorontsov, R. Voskoboinikov, C. Rae, Shearing of γ' precipitates in Ni-base superalloys: a phase field study incorporating the effective γ-surface, Philos. Mag. 92 (2012) 608–634, https://doi.org/10.1080/14786435.2011.630691.